Journal of Applied Electrochemistry **29**: 1263–1275, 1999.

An electric model of a vapour anode, multitube alkali–metal thermal-to-electric converter

J.-M. TOURNIER and M.S. EL-GENK*
Institute for Space and Nuclear Power Studies/Department of Chemical and Nuclear Engineering, School of Engineering, The University of New Mexico, Albuquerque, NM 87131, USA
*(*author for correspondence, e-mail: mgenk@unm.edu)*

Received 22 October 1998; accepted in revised form 16 March 1999

Key words: alkali–metal thermal-to-electric converter, beta″-alumina solid electrolyte, electric model, multitube cell, vapour anode

Abstract

A two-dimensional electric model of vapour anode, multitube alkali–metal thermal-to-electric conversion (AMTEC) cells was developed. These cells are being developed to power the Pluto/Kuiper Express and Europa Orbiter spacecrafts, at NASA which are scheduled for launch early in the next century. Model results of several cells tested at the Air Force Research Laboratory showed that electric losses in the current collector networks and the connecting leads were negligible. The charge-exchange polarization/concentration losses in the TiN electrodes were the major losses, amounting to 25–50% of the cell's total theoretical power, while the contact losses and the beta″-alumina solid electrolyte ionic losses amounted to less than 16% of the cell theoretical power. Results also showed that a cell with advanced Rh_2W electrodes could have delivered from 14% to 25% more electrical power.

List of symbols

A	cross-section area (m^2)
B	temperature-independent, charge-exchange coefficient (A $K^{1/2}$ Pa^{-1} m^{-2})
d_{bus}	bus wire diameter (m)
F	Faraday constant (96 485 C mol^{-1})
f_B	Faraday coefficient, $f_B = F/(R_g T_B)$ (C J^{-1})
G	dimensionless geometric factor for vapour pressure losses
H	height of electrode axial segments (m)
h	wire-screen mesh size (m)
I	electrical current (A)
J	electrical (radial) current density (A m^{-2})
J^{ex}	charge-exchange current density (A m^{-2})
J^{ex}_{sat}	saturated equilibrium, charge-exchange current density (A m^{-2})
L_E	length of BASE electrodes (m)
L_{rings}	length of helical wire per axial segment, Equation 11 (m)
N	number of electrode axial segments
N_p	number of mesh wires per half circumference of BASE tube, Equation 9
N_{rings}	number of helical wire rings per axial segment, Equation 11
N_S	number of seried-connected BASE tubes
N_{wires}	number of mesh wires per axial segment, Equation 9
P	pressure (Pa)
R	electrical resistance (Ω)
R_g	perfect gas constant (8.314 J mol^{-1} K^{-1})
R_{int}	internal resistance of AMTEC cell (Ω)
R_L	external load resistance (Ω)
R_{leak}	leakage resistance of BASE braze joint (Ω)
R_o	equivalent external load per BASE tube (Ω)
R'_B	BASE ionic resistance (Ω m^2)
R'_{cont}	contact resistance between BASE/electrode/current collector (Ω m^2)
r	outer radius (m)
T	temperature (K)
t	thickness (m)
V	electrical voltage (V)

Greek letters

α	electrochemical transfer coefficient, $\alpha = 1/2$
ΔT	temperature margin (temperature difference between BASE tube cold end and evaporator)
ε	volume porosity
ζ	concentration and charge-exchange polarization losses (V)
ρ	electrical/ionic resistivity (Ω m)

Subscripts/superscripts

a	anode
B	Beta″-alumina solid electrolyte (BASE)
bus	axial bus wire
c	cathode
cc	closed-circuit
cd	cell cold end (condenser)
conn	BASE tubes connector lead
E	porous cathode electrode
ex	charge-exchange

hot	cell hot end
lead	connector lead
mesh	wire screen mesh
o	effective electromotive force
oc	open circuit
r	radial
sat	liquid–vapour saturation line
sheet	electrode sheet
sp	metal sponge
w	wire
wire	tie wire
z	axial
θ	circumferential

1. Introduction

A comprehensive testing and modelling program is underway at the Air Force Research Laboratory (AFRL) Space Vehicles Directorate [1], jointly with the University of New Mexico Institute for Space and Nuclear Power Studies (UNM–ISNPS). The objective of this program is to advance the technology of vapour anode, multitube alkali–metal thermal-to-electric converters (AMTECs) for flight on future space missions. These AMTEC cells are also being developed for flight on the NASA Pluto/Kuiper Express (PX) and Europa Orbiter missions, scheduled for launch early in the next century [1–3]. Each vapour anode, multitube PX-series AMTEC cell has between 5 and 7 beta″-alumina solid electrolyte (BASE) tubes, connected electrically in series. Each BASE tube has a total of 6 cm^2 of electrode surface area (Figures 1 and 2). The TiN anode and cathode porous electrodes are covered with molybdenum mesh current collectors, to minimize internal electric losses. Further details on the design of the PX-series cells and test results can be found elsewhere [1–3].

An integrated AMTEC performance and evaluation analysis model (APEAM) has also been developed, to support ongoing tests at AFRL and evaluate the performance of PX-type AMTEC cells. This integrated cell model consists of four major components: (a) a sodium vapour pressure loss model, which calculates the sodium vapour pressure at the interfaces between the cathode electrode and the BASE tube [4]; (b) a radiation–conduction heat transfer model, which accounts for all heat exchanges between the different components of the cell and calculates the temperatures throughout the cell [5]; (c) a cell electrochemical model, which calculates the effective potential developed across the BASE, due to the isothermal expansion of sodium ions; and (d) a two-dimensional cell electric circuit model, which determines the electrical resistances of the BASE, electrodes, current collectors and conductor leads to the external load, and calculates the cell electrical potentials, electrode current density and the total electrical current

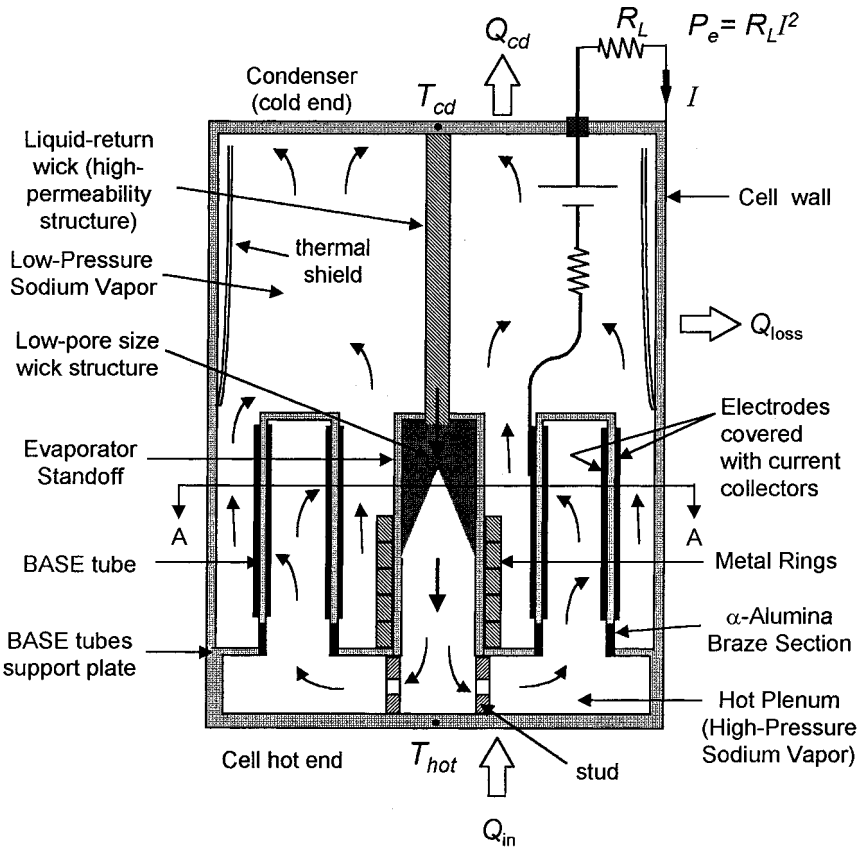

Fig. 1. Cross section of a PX-type cell (not to scale).

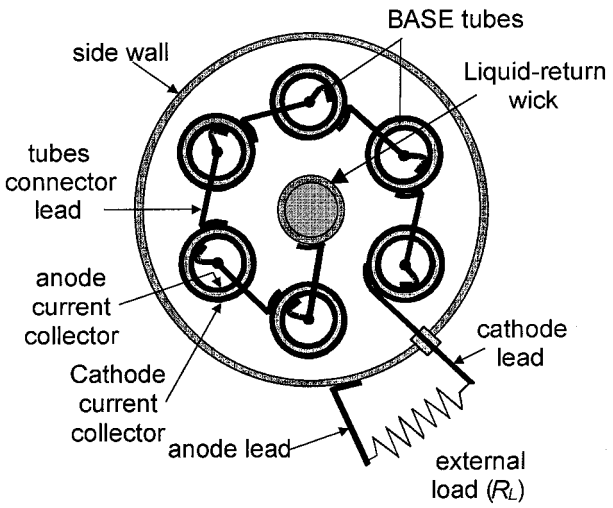

Fig. 2. Plan view of a PX-type cell taken at section A–A from Figure 1.

of the cell. The latter model is described in detail in the following Section. This model is also used to evaluate the contribution of the various electrical loss processes in the PX-series cells. The results of the effects of BASE/electrode/current collector contact resistance, charge-exchange current and BASE tube leakage resistance on the PX-3G cell performance are analysed and discussed.

2. Electric model

The two-dimensional electric model of vapour anode, multitube AMTEC cells includes four options of current collector configurations (Figure 3). The model accounts for the effects of nonuniform axial temperature and sodium vapour pressure profiles along the BASE tubes/cathode electrodes, and predicts the radial and axial electrical losses in the current collector network. This model is coupled to the other submodels in APEAM, and is used to evaluate the contributions of the various components of the internal electric losses in the cell. Internal electric losses are those due to the following: (a) concentration and charge-exchange polarization losses at the BASE/electrodes interfaces; (b) BASE ionic resistance; (c) contact resistances between BASE/electrode and electrode/current collector; (d) sheet resistance of the electrodes; (e) resistances of current collectors, bus wires and conductor leads to the external load; and (f) resistance to leakage current between the anode and cathode electrodes through the BASE metal–ceramic braze joints. These joints link the BASE tubes to the metal support plate of the cell and must be highly conductive to heat but highly resistive to electric current. Electric losses in a typical AMTEC cell are all accounted for in the present model and are discussed separately in the following subsections.

2.1. *Open-circuit voltage and polarization losses*

Neglecting the Seebeck voltage, generated by the radial temperature gradient across the BASE, the effective electromotive force of the cell is given by

$$V_{\mathrm{o}}^{\mathrm{cc}} = V^{\mathrm{oc}} - \zeta_{\mathrm{a}} - (-\zeta_{\mathrm{c}}) \tag{1}$$

The open-circuit voltage, V^{oc}, is proportional to the isothermal expansion work of sodium ions in the BASE tubes, and is given by the Nernst equation [6]:

$$V^{\mathrm{oc}} = \frac{R_{\mathrm{g}}T_{\mathrm{B}}}{F}\ln\left[P_{\mathrm{a}}^{\mathrm{oc}}/P_{\mathrm{c}}^{\mathrm{oc}}\right] = \frac{1}{f_{\mathrm{B}}}\ln\left[P_{\mathrm{a}}^{\mathrm{oc}}/P_{\mathrm{c}}^{\mathrm{oc}}\right] \tag{2}$$

The concentration and charge-exchange polarization overpotentials at the anode and cathode are given by the Butler–Volmer equation [7, 8]:

$$\frac{J_i}{J_i^{\mathrm{ex}}} = \exp[-\alpha f_{\mathrm{B}}\zeta_i] - \frac{P_i^{\mathrm{cc}}}{P_i^{\mathrm{oc}}}\exp[(1-\alpha)f_{\mathrm{B}}\zeta_i] \tag{3a}$$

The subscript 'i' in Equation 3(a) stands for either 'a' (anode) or 'c' (cathode). For a symmetric barrier, the electrochemical transfer coefficient $\alpha = 1/2$, and Equation 3(a) can be inverted to give the polarization overpotential explicitly in terms of the cell current density:

$$\zeta_i = -\frac{2R_{\mathrm{g}}T_{\mathrm{B}}}{F}\ln\left\{\frac{1}{2}\left[\left(\frac{J_i}{J_i^{\mathrm{ex}}}\right)^2 + 4\frac{P_i^{\mathrm{cc}}}{P_i^{\mathrm{oc}}}\right]^{1/2} + \frac{1}{2}\frac{J_i}{J_i^{\mathrm{ex}}}\right\} \tag{3b}$$

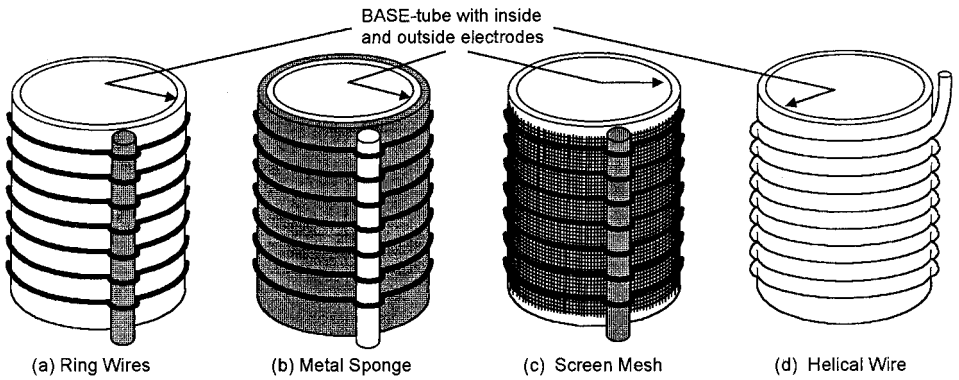

Fig. 3. Current collector designs in vapour anode, multitube AMTEC cell.

The overpotential, ζ_i increases logarithmically with the cell current, reducing the voltage potential across the BASE. In Equation 3(b), $\zeta_c < 0$, $\zeta_a > 0$, and $J_c = -J_a$ for a thin BASE membrane. The charge-exchange current densities, J_i^{ex}, a measure of the effective local conductance at the BASE/electrode/sodium vapour triple phase boundary, are related to the saturated equilibrium exchange-current density, J_{sat}^{ex}, as [7, 8]:

$$J_i^{ex} = J_{sat}^{ex}\left[\frac{P_i^{oc}}{P_{sat}(T_B)}\right]^{\alpha} \tag{4a}$$

Since the sodium vapour pressure at the cathode ($P_c^{cc} < 50$ Pa) is several orders of magnitude smaller than that at the anode ($P_a^{cc} \sim 15$–60 kPa), the anode exchange-current density is much larger than the cathode exchange-current density, hence the polarization overpotential on the anode side, ζ_a, is negligible. Experimental investigations have shown that the saturated equilibrium exchange-current density, J_{sat}^{ex}, is essentially a function of the BASE temperature and of the type of electrodes. It can be expressed as [7, 8]

$$J_{sat}^{ex} = B \times \frac{P_{sat}(T_B)}{\sqrt{T_B}} \tag{4b}$$

where B is the temperature-independent charge-exchange coefficient, expressed in units of A $K^{1/2}$ Pa^{-1} m^{-2}. As a result,

$$J_i^{ex} = B \times \left[P_i^{oc} P_{sat}(T_B)/T_B\right]^{1/2} \tag{4c}$$

As shown in Equation 3(b), the concentration losses, or the effect of increased pressure at the BASE/cathode electrode interface (due to sodium vapour pressure losses in the low pressure cavity of the cell, Figure 1a), increase with cell current or sodium flow rate. The pressure drop across the cathode electrode is expressed in terms of an empirical dimensionless factor G_E. Both B and G_E are characteristic of the type of electrodes used, and are determined experimentally. Typical TiN electrodes have $B \sim 80$ A $K^{1/2}$ Pa^{-1} m^{-2} and $G_E \sim 50$ [9].

When the charge-exchange polarization losses are negligible (i.e., B is infinite), the Nernst electromotive force of the AMTEC cell is reduced only by the concentration losses, and is proportional to the expansion work by sodium ions through the BASE, under load. That is,

$$V_o^{cc} = \frac{1}{f_B}\ln\left[P_a^{cc}/P_c^{cc}\right] \tag{5}$$

2.2. *BASE ionic resistance*

The BASE ionic resistance is given by

$$R'_B = \rho_B \times r_B \ln[r_B/(r_B - t_B)] \tag{6}$$

and reduces to $R'_B = \rho_B \times t_B$, when $t_B \ll r_B$. Ionic resistance is directly proportional to the BASE tube thickness. The PX-series cells use cylindrical BASE tubes having an outer radius, $r_B = 3.81$ mm, and a thickness, $t_B = 0.508$ mm. This thickness is a compromise between performance (requiring a thinner wall) and structural strength (requiring a thicker wall) of the ceramic BASE tubes.

2.3. *Current collector losses*

For large electrode area, current collection while maintaining high electrode performance is a design and modelling challenge. The electronic sheet resistance of the metal electrode could be significant and must be compensated for with the use of highly conductive current collector networks. High-conductivity thin porous electrodes can be fabricated by decreasing their volume porosity or increasing their thickness, but at the expense of increased flow resistance to the sodium vapour (i.e., higher G_E). Current collectors which properly contact the BASE electrodes, without significantly reducing the electrode surface area, must be designed to minimize ohmic loss, by providing the shortest current flow path from any point on the BASE electrode surface to the electric leads of the cell. This is accomplished through the use of a metal sponge or a metal wire grid that provides both current pick-up points from the electrode and axial current transport at low ohmic losses [10].

To calculate the electrodes sheet resistances, and the resistances of the current collectors and the buses, a two-dimensional electric model was developed. This model can handle any of four different current collector configurations typically used in vapour anode, multitube AMTEC cells [10, 11]. The first configuration (Figure 3(a)) consists of tie wires wrapped around the BASE tube cathode electrode, and connected to a larger axial bus. The second is a metal sponge wrapped around the BASE tube cathode electrode and held in place by tie wires connected to an axial bus (Figure 3(b)). The third consists of one layer of wire screen mesh wrapped around the BASE tube cathode electrode and held in place by tie wires connected to an axial bus (Figure 3(c)). The fourth is a single wire wrapped around the BASE tube cathode electrode as a helix (Figure 3(d)).

The two-dimensional electric model of these current collector networks discretized the BASE tube/electrodes/current collectors system into N axial segments of equal height, H (Figure 4). Every axial segment k provides an effective electromotive force V_k^o (Equation 1), and its resistance, R_k, includes the BASE ionic resistance, contact resistances between the current collectors and electrodes, sheet resistances of the electrodes, and radial/circumferential resistances of the current collectors. The ohmic resistances R_k^a and R_k^c are the axial resistances of the anode and cathode current collectors, respectively. The resistance R_o in segment $k = 0$ (Figure 4) is the equivalent external load per BASE tube.

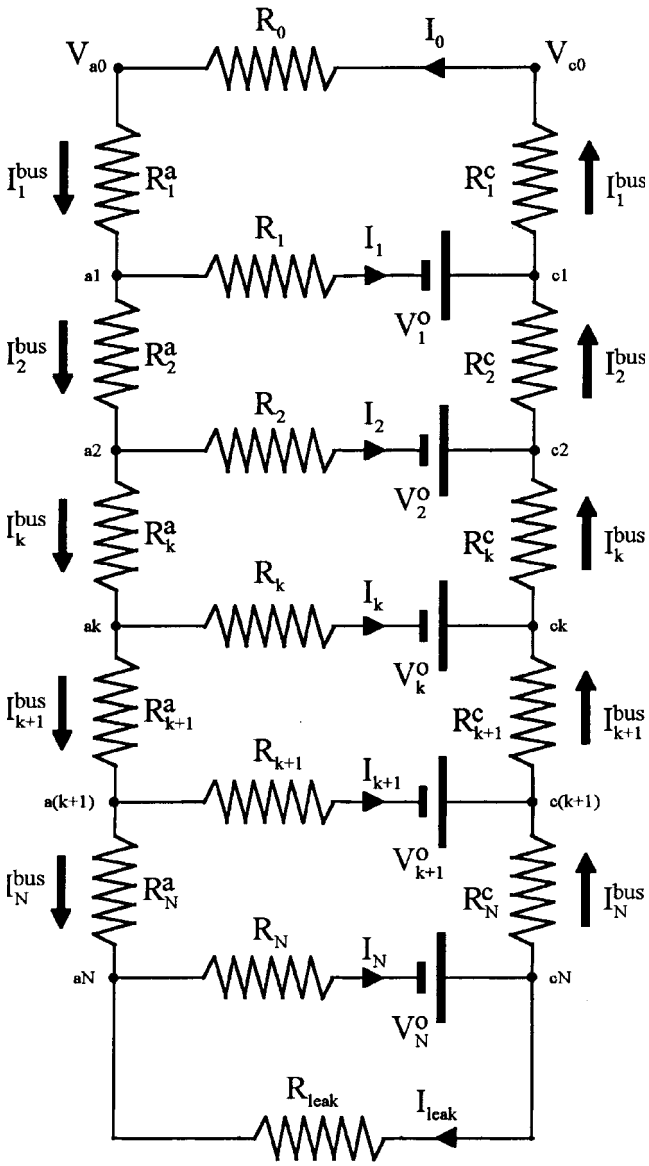

Fig. 4. Electric circuit model of BASE tube current collectors.

Finally, R_{leak} is the leakage resistance between the anode and cathode electrodes, through the BASE metal-to-ceramic braze joint (Figure 1). This leakage path is treated as segment number $(N+1)$ in the model.

The problem of current collection is truly three-dimensional and calculations of local current density and electric potential can be carried out using finite elements techniques and integrating over the electrode surface and the current collector grid elements [11]. A current collection path was assumed, from the BASE surface through the electrode and the collector network components. The corresponding ohmic resistances R_k, R_k^{a} and R_k^{c} were obtained by integrating the Joule losses along the conduction path [10]. Since electrons travel along the path of least resistance, the approach of selecting a given, probable conduction path is conservative. Calculational results obtained for the resistances of each current collector type in Figure 3 are given next.

2.4. *Ring wires in contact with axial bus*

In this configuration (Figure 3(a)), it is assumed that electrons travel axially through the electrode (sheet resistance) to the nearest wire of the current collector, then travel circumferentially through the ring to the contact point with the axial bus. The latter collects current at the different contact points with the tie wires, which are separated by a distance H. For this collection path, we obtain

$$R_k = \frac{R'_{\text{B}} + R^{\text{a}'}_{\text{cont}} + R^{\text{c}'}_{\text{cont}}}{[2\pi r_{\text{B}} H]} + R^{\text{E,z}}_{\text{sheet}} + R^{\theta}_{\text{wire}} \tag{7a}$$

where

$$R^{\text{E,z}}_{\text{sheet}} = \frac{H^2}{12}\frac{\rho_{\text{E}}}{t_{\text{E}}(1-\varepsilon_{\text{E}})} \times \frac{1}{[2\pi r_{\text{B}} H]} \tag{7b}$$

and

$$R^{\theta}_{\text{wire}} = \frac{\rho_{\text{w}}}{A_{\text{w}}}\left[\frac{2\pi(r_{\text{B}} + r_{\text{w}})}{12}\right] \tag{7c}$$

The axial resistance of a bus section of height H is simply

$$R^{\text{bus}}_k = \frac{\rho_{\text{bus}}}{A_{\text{bus}}} H \tag{7d}$$

2.5. *Metal sponge in contact with axial bus*

In this configuration (Figure 3(b)), it is assumed that electrons travel radially through the electrode to the metal sponge, then travel circumferentially through the sponge to the nearest contact point with the axial bus. In this case,

$$R_k = \frac{R'_{\text{B}} + R^{\text{a}'}_{\text{cont}} + R^{\text{c}'}_{\text{cont}}}{[2\pi r_{\text{B}} H]} + R^{\text{E,r}}_{\text{sheet}} + R^{\text{r}}_{\text{sponge}} + R^{\theta}_{\text{sponge}} \tag{8a}$$

where

$$R^{\text{E,r}}_{\text{sheet}} = \frac{\rho_{\text{E}} t_{\text{E}}}{(1-\varepsilon_{\text{E}})} \times \frac{1}{[2\pi r_{\text{B}} H]} \tag{8b}$$

$$R^{\text{r}}_{\text{sponge}} = \frac{\rho_{\text{sp}} t_{\text{sp}}}{2(1-\varepsilon_{\text{sp}})} \times \frac{1}{[2\pi r_{\text{B}} H]} \tag{8c}$$

and

$$R^{\theta}_{\text{sponge}} = \frac{\rho_{\text{sp}}}{t_{\text{sp}}(1-\varepsilon_{\text{sp}})H} \times \frac{2\pi(r_{\text{B}} + t_{\text{sp}}/2)}{12} \tag{8d}$$

The axial bus continuously collects electrons along its length, and the resistance of a segment k of the bus is given as

$$R_k^{\text{bus}} = \frac{\rho_{\text{bus}} H}{A_{\text{bus}}} \left[\frac{I_{k+1}^{\text{bus}}}{I_k^{\text{bus}}} + \frac{1}{3} \left(1 - \frac{I_{k+1}^{\text{bus}}}{I_k^{\text{bus}}} \right)^2 \right] \tag{8e}$$

With a large number of axial sections ($N > 20$), only a few iterations were needed for the convergence of the solution (to resolve the dependence of R_k^{bus} on the currents).

2.6. *Screen mesh in contact with axial bus*

In this more involved configuration (Figure 3(c)), electrons flow axially and circumferentially through the electrode to the nearest mesh grid segment of the current collector, then travel to the nearest horizontal grid segment, which conducts them to the nearest contact point with the axial bus (Figure 5). Since the screen mesh is a good conducting structure, the conduction through the tie wires was neglected in this analysis. Resulting equations were integrated over $H \gg h$ (h is the mesh size). Introducing N_{wires} and N_{p} such that

$$H = h \times N_{\text{wires}} \quad \text{and} \quad \frac{2\pi r_{\text{B}}}{h} = 2(N_{\text{p}} + 1) \tag{9}$$

we obtained

$$R_k = \frac{R'_{\text{B}} + R_{\text{cont}}^{\text{a}'} + R_{\text{cont}}^{\text{c}'}}{[2\pi r_{\text{B}} H]} + R_{\text{sheet}}^{\text{E}} + R_{\text{mesh}}^{\text{z}} + R_{\text{mesh}}^{\theta} \tag{10a}$$

where

$$R_{\text{sheet}}^{\text{E}} = \frac{h^2}{24} \frac{\rho_{\text{E}}}{t_{\text{E}}(1 - \varepsilon_{\text{E}})} \times \frac{1}{[2\pi r_{\text{B}} H]} \tag{10b}$$

$$R_{\text{mesh}}^{\text{z}} + R_{\text{mesh}}^{\theta} = \frac{h^3}{30} \frac{\rho_{\text{w}}^{\text{mesh}}}{A_{\text{w}}^{\text{mesh}}} (1 + \alpha) \times \frac{1}{[2\pi r_{\text{B}} H]} \tag{10c}$$

and

$$\alpha = \frac{1}{N_{\text{p}} + 1} \left[10N_{\text{p}}^3 + 30N_{\text{p}}^2 + 31N_{\text{p}} + 11 \right] \tag{10d}$$

The axial bus collects current at the contact points with the grid mesh (Figure 5), and its resistance is given as

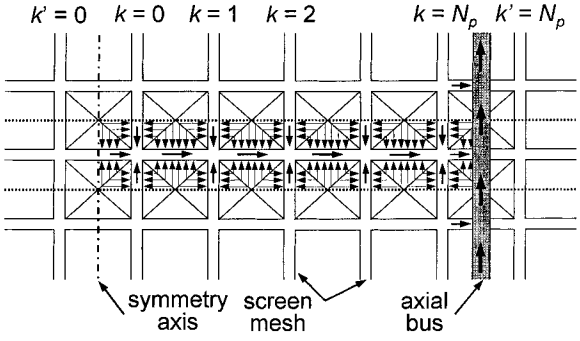

Fig. 5. Electrons conduction path in a screen mesh current collector.

$$R_k^{\text{bus}} = \frac{\rho_{\text{bus}} H}{A_{\text{bus}}} \left[\frac{I_{k+1}^{\text{bus}}}{I_k^{\text{bus}}} + \frac{1}{3} \left(1 + \frac{1}{2N_{\text{wires}}^2} \right) \left(1 - \frac{I_{k+1}^{\text{bus}}}{I_k^{\text{bus}}} \right)^2 \right] \tag{10e}$$

2.7. *Wrapped helical wire*

In this configuration (Figure 3(d)), a bus wire of radius r_{bus} is tightly wrapped around the BASE tube. The angle of the helix is assumed to be small. Electrons travel axially through the electrode to the nearest wire contact line of the current collector, then circumferentially through the helical wire. Resulting equations were integrated over $H > r_{\text{bus}}$. Introducing N_{rings}, L_{rings} and A_{bus} such that

$$H = 2r_{\text{bus}} \times N_{\text{rings}} \tag{11a}$$

$$L_{\text{rings}} = 2\pi(r_{\text{B}} + r_{\text{bus}}) \times N_{\text{rings}} \tag{11b}$$

$$A_{\text{bus}} = \pi r_{\text{bus}}^2 \tag{11c}$$

we obtained

$$R_k = \frac{R'_{\text{B}} + R_{\text{cont}}^{\text{a}'} + R_{\text{cont}}^{\text{c}'}}{[2\pi r_{\text{B}} H]} + R_{\text{sheet}}^{\text{E,z}} \tag{12a}$$

where

$$R_{\text{sheet}}^{\text{E,z}} = \frac{r_{\text{bus}}^2}{3} \frac{\rho_{\text{E}}}{t_{\text{E}}(1 - \varepsilon_{\text{E}})} \times \frac{1}{[2\pi r_{\text{B}} H]} \tag{12b}$$

and

$$R_k^{\text{bus}} = \frac{\rho_{\text{bus}} L_{\text{rings}}}{A_{\text{bus}}} \left[\frac{I_{k+1}^{\text{bus}}}{I_k^{\text{bus}}} + \frac{1}{3} \left(1 - \frac{I_{k+1}^{\text{bus}}}{I_k^{\text{bus}}} \right)^2 \right] \tag{12c}$$

2.8. *Calculation of electric current and voltage*

The conservation of current at the nodes of the electric circuit of the BASE/electrode/current collector system in Figure 4 shows that the current travelling down the anode collector is equal to that travelling up the cathode collector. The electric currents at the nodes of the electric circuit in Figure 4 were determined from Kirchhoff's law. The electronic leakage path is treated as an additional branch $(N+1)$ with

$$R_{N+1} = R_{\text{leak}} \tag{13a}$$

$$R_{N+1}^{\text{a}} = R_{N+1}^{\text{c}} = 0 \tag{13b}$$

$$V_{N+1}^{\text{o}} = 0 \tag{13c}$$

When applied to the closed circuit between the load and the kth branch, Kirchhoff's law is written as

$$V_k^{\mathrm{o}} = R_{\mathrm{o}} I_{\mathrm{o}} + R_k I_k + \sum_{i=1}^{k} (R_i^{\mathrm{c}} + R_i^{\mathrm{a}}) \times I_i^{\mathrm{bus}} \tag{14}$$

Since $I_{\mathrm{o}} = I_1^{\mathrm{bus}}$ and $I_k = I_k^{\mathrm{bus}} - I_{k+1}^{\mathrm{bus}}$, one obtains:

$$V_k^{\mathrm{o}} = R_{\mathrm{o}} I_1^{\mathrm{bus}} + R_k (I_k^{\mathrm{bus}} - I_{k+1}^{\mathrm{bus}}) + \sum_{i=1}^{k} (R_i^{\mathrm{c}} + R_i^{\mathrm{a}}) \times I_i^{\mathrm{bus}} \tag{15}$$

for $k = 1$ to $(N+1)$. Note that $I_{N+2}^{\mathrm{bus}} = 0$.

Equation 15 represent a linear system of $(N+1) \times (N+1)$ relations that were solved for the unknowns $\{I_k^{\mathrm{bus}}\}$, $k = 1$ to $N+1$, using a simple Gauss elimination algorithm. To improve the convergence of the iterative solution, the concentration and charge-exchange overpotentials that appear in the effective electromotive forces V_k^{o} (Equation 1) were linearized in terms of branch current $I_k = I_k^{\mathrm{bus}} - I_{k+1}^{\mathrm{bus}}$, using Equation 3(b) [12].

2.9. *Equivalent external load resistance*

Because of the symmetry in the AMTEC cell, and to a good approximation, the BASE tubes have identical temperature, sodium vapour pressure and current density axial distributions. Since the N_{S} BASE tubes in the cell are connected electrically in series, every tube contributes an equal voltage to the load. Figures 6 and 7 show schematics of the equivalent electrical circuit in the cell. The cathode end of BASE tube k is connected to the anode of the next tube $(k+1)$ through a connector lead of resistance $R_{\mathrm{lead}}^{\mathrm{conn}}$. The anode of the first tube and cathode of the last tube are connected to the external load through leads of resistances $R_{\mathrm{lead}}^{\mathrm{a}}$ and $R_{\mathrm{lead}}^{\mathrm{c}}$, respectively. Since

$$V_1^{\mathrm{c}} - V_1^{\mathrm{a}} = \cdots = V_k^{\mathrm{c}} - V_k^{\mathrm{a}} = \cdots = V_{N_{\mathrm{S}}}^{\mathrm{c}} - V_{N_{\mathrm{S}}}^{\mathrm{a}} = V^{\mathrm{c}} - V^{\mathrm{a}} \tag{16}$$

Kirchhoff's law applied to the circuit in Figure 7 gives

$$N_{\mathrm{S}}(V^{\mathrm{c}} - V^{\mathrm{a}}) = \{(N_{\mathrm{S}} - 1) R_{\mathrm{lead}}^{\mathrm{conn}} + R_{\mathrm{lead}}^{\mathrm{a}} + R_{\mathrm{lead}}^{\mathrm{c}} + R_{\mathrm{L}}\} I_{\mathrm{o}} \tag{17}$$

Since $V^{\mathrm{c}} - V^{\mathrm{a}} = R_{\mathrm{o}} I_{\mathrm{o}}$ by definition (Figure 4), the effective external load resistance per BASE tube can be expressed as

$$R_{\mathrm{o}} = \{(N_{\mathrm{S}} - 1) R_{\mathrm{lead}}^{\mathrm{conn}} + R_{\mathrm{lead}}^{\mathrm{a}} + R_{\mathrm{lead}}^{\mathrm{c}} + R_{\mathrm{L}}\} / N_{\mathrm{S}} \tag{18}$$

In the present electric model, the electrical resistances of the electrodes and current collectors were taken to be temperature-dependent. The ionic resistivity of the Na-BASE, ρ_{B}, was calculated using the following relation [13]:

$$\rho_{\mathrm{B}} = T_{\mathrm{B}} \times \left(1.62 \times 10^{-5} \times \exp[-45.5/T_{\mathrm{B}}] + 1.55 \times 10^{-7} \times \exp[3722/T_{\mathrm{B}}]\right) \tag{19}$$

3. Results and discussion

The present electric model was integrated into a full cell model, APEAM, and an efficient numerical procedure was developed to resolve the couplings between the various models of the different physical processes in the cell [12]. The axial distributions of the sodium vapour pressure along the electrodes and of the BASE temperature were obtained from the sodium vapour pressure loss model and heat transfer model, respectively. Analysis of the results showed that, except for a thick sponge collector, all current collectors investigated performed extremely well, with insignificant internal losses. These current collectors provide enough contact points with the electrodes, reducing the sheet resistances in the electrodes.

The fully-integrated cell model (APEAM) has been extensively benchmarked with experimental data of the

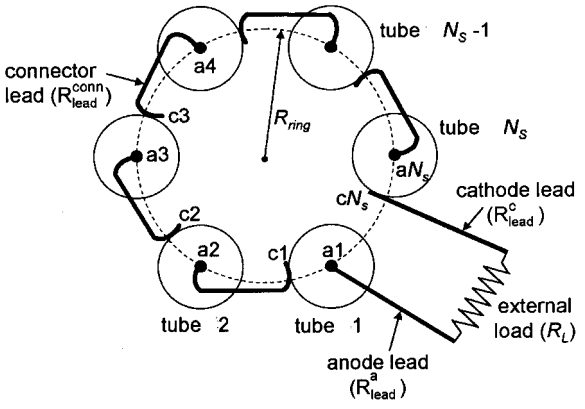

Fig. 6. Electrical connection of BASE tubes and external load in PX-series cell.

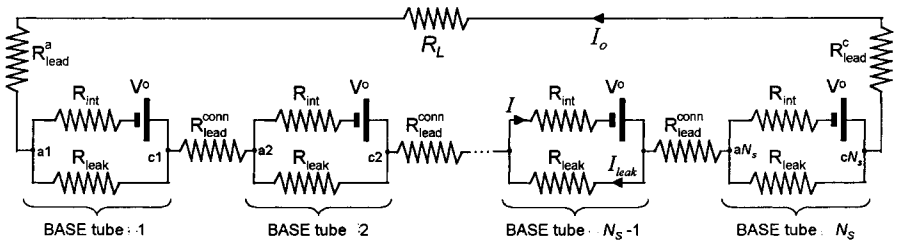

Fig. 7. Electric circuit model of BASE tubes and external load in PX-series cell.

cells tested at AFRL [1–3, 12]. The design parameters for a number of cells, and those relevant to the cell electric model, such as current collector designs, are given in Table 1. All the PX-series cells listed in Table 1 have been tested in vacuum at AFRL. This Table also lists the values of the estimated cathode electrode geometric factor for pressure drop, G_E, contact resistance between electrode and current collector, $R'_{cont} = R^{a'}_{cont} = R^{c'}_{cont}$, charge-exchange coefficient, B, and leakage resistance of the metal–ceramic braze joint between BASE tube and SS support plate, R_{leak}, that were used in the model for best comparison with test data. To compare the electric losses in the cell, the corresponding voltage losses are expressed as a fraction of the theoretical Nernst electrical power of the cell:

$$P_{Nernst} = N_S \times (2\pi r_B) \int_{z=0}^{L_E} V^{oc}(z) \cdot J(z)\, dz \approx N_S \times \sum_{k=1}^{N} V_k^{oc} I_k \quad (20)$$

This electric power equals that delivered to the external load plus the sum of all internal and lead losses. The main contributors to the internal electrical losses in the

Table 1. Electrical losses in PX-series cells near their peak electric power

Parameters	PX-2C	PX-4C	PX-5A	PX-3G[a]	PX-3A
Cell design					
Number of BASE tubes	7	6	6	6	5
Cathode electrode/tube (mm^2)	600	600	600	600	600
Current collectors	100 mesh Cu	50 mesh Mo	50 mesh Mo	60 mesh Mo	60 mesh Mo
Mesh wire diameter	110 μm	210 μm	210 μm	163 μm	178 μm
Bus wire cross-section area (mm^2)	0.503 (Cu)	0.503 (Mo)	0.503 (Mo)	0.806 (Ta)	0.503 (Mo)
Electrode geometric factor, G_E	12	50	50	50	50
Contact resistance, R'_{cont} (Ω cm^2)	0.08	0.06	0.06	0.06	0.06
Exchange current, B (A $K^{1/2}$ Pa^{-1} m^{-2})	120	120	120	75	120
Leakage resistance, R_{leak} (Ω)	$+\infty$	$+\infty$	$+\infty$	3.0	5.0
Cell performance					
External load (Ω)	2.0	1.2	1.2	1.14	0.65
Cell current (A)	1.47	1.763	1.759	1.798	2.67
External load electric power (W_e)	4.39	3.73	3.71	3.69	4.64
Cell conversion efficiency	11.2%	10.7%	11.8%	12.8%	14.2%
Leakage current, I_{leak} (A)	0.0	0.0	0.0	0.121	0.079
Cell heat input (W_{th})	39.0	34.9	31.5	28.90	32.7
Wall heat losses (W_{th})	6.5	6.7	7.1	1.95	6.1
Open-circuit voltage (V)	6.33	4.57	3.58	5.10	3.61
Concentr./polarization losses (V)	2.84	1.87	0.89	2.45	1.11
Cell internal resistance (Ω)	0.348	0.285	0.285	0.274	0.240
Anode pressure (kPa)	14.7	12.7	13.2	17.2	33.2
Cathode pressure (Pa)	16.2	24.3	30.4	26.7	48.0
Cell's Nernst electrical power (W_e)	9.42	8.09	6.33	9.76	9.97
Nernst electrical power fractions					
External load resistance (%)	46.5	46.1	58.7	37.7	46.6
Concentration/polarization (%)	45.0	41.1	25.0	48.4	30.8
Contact resistance (%)	4.6	4.9	6.2	4.8	8.1
BASE ionic resistance (%)	3.2	4.5	5.8	4.4	7.5
Electrons leakage (%)	0.0	0.0	0.0	2.7	1.5
Current collectors (%)	0.4	2.0	2.5	1.2	3.3
BASE tubes connecting leads (%)	0.3	1.4	1.8	0.8	2.2
Temperatures (K)					
Hot end, T_{hot}	1127	1130	1123	1123	1173
BASE brazes (maximum)	1097	1092	1089	1094	1140
Hot end of electrodes	1037	1036	1042	1051	1123
Cold end of electrodes	1002	988	1000	1012	1060
Cold end of BASE tubes	1000	986	997	1010	1055
Evaporator, T_{ev}	979	966	969	990	1044
Margin, ΔT	+21 K	+20 K	+28 K	+20 K	+11 K
Cold end, T_{cd}	529	565	623	553	623
Initial test date	12/24/96	3/1/97	5/1/97	11/4/97	7/9/97
Operation (h)	600	1800	672	3000	11 000

[a] PX-3G cell 1 in 8-cell ground-demo system.

cells, in an order of decreasing importance, were found to be: (a) concentration/charge-exchange polarization losses on the cathode side; (b) contact losses between current collectors and metal electrodes; (c) BASE ionic resistance; and (d) electrons leakage between anode and cathode electrodes. In all cases, the Joule losses in the current collector networks and in the connecting leads between the BASE tubes amounted to less than 6% of the Nernst power of the cell (Table 1). The polarization/ concentration losses of the TiN electrodes were the major losses, amounting to 25–50% of the Nernst power. The contact losses were a distant second, amounting to less than 9%. When combined together with the BASE ionic resistance losses, they amounted to less than 16% of the Nernst power in all cells in Table 1.

The effect of changing the external load resistance (or the cell electrical current) on the weighting of the different electrical losses in the cell is illustrated in Figure 8. This Figure shows that for the PX-3G cell, which operated at hot side and cold side temperatures of 1123 K and 553 K, respectively, the charge-exchange/ concentration losses increased logarithmically with cell current (also see Figure 14(c)). However, the internal ohmic losses (contact losses, ionic losses in BASE tube, current collectors and connecting leads losses) increased linearly with the cell electrical current (Figure 8). The leakage losses were large at low electrical current (high voltage), but decreased very rapidly with increasing current, since they are proportional to the square root of the electrolyte's voltage differential (Figure 13(b)).

When the cell current, $I = 0.7$ A, the fraction of the Nernst electric power delivered to the external load peaked at 48% (Figure 8). However, since the theoretical Nernst power increases with increasing cell current (Equation 20, and Figure 9), the absolute value of the load electrical power peaked at a higher cell current $I = 1.8$ A (Figure 12(a)). The load peak electric power amounted to only 36% of the Nernst power of the cell. Note that the open-circuit theoretical Nernst power does not equal zero (when the electrical current through the load, $I = 0$), because of the leakage current through the brazes of the BASE tubes. When $I = 0$ (open-circuit), $I_{leak} = 0.27$ A (Figure 13(c), for $R_{leak} = 3\,\Omega$) and the theoretical Nernst power of the cell equals the electrical power losses in the leakage resistances: $P_{Nernst} = N_S \times R_{leak} I_{leak}^2 = 1.3\,W_e$ (Figure 9).

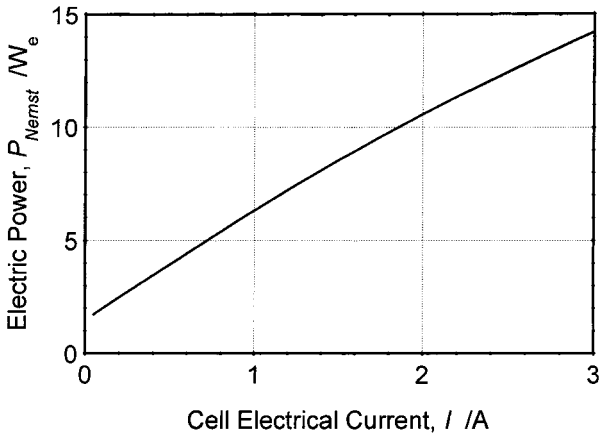

Fig. 9. Theoretical Nernst power in PX-3G cell. $T_{hot} = 1123$ K and $T_{cd} = 553$ K.

3.1. *Sodium vapour pressure and current density in PX-3G*

Figure 10 shows the calculated vapour pressure distribution on the cathode (low-pressure) side of the PX-3G cell. The pressure profile along the BASE tubes is typically parabolic, due to the continuous vapour addition along the BASE outer surface. As expected, the sodium vapour pressure drop on the cathode side increases with increasing cell current, or vapor mass flow rate [4]. At a cell current of 1.8 A, the sodium vapour pressure along the BASE/cathode electrode interface varied between 24 Pa and 30 Pa. There was a 6.7 Pa pressure drop across the cathode electrode, and a 5.3 Pa pressure drop at the BASE/cathode electrode interface due to evaporation of sodium vapour.

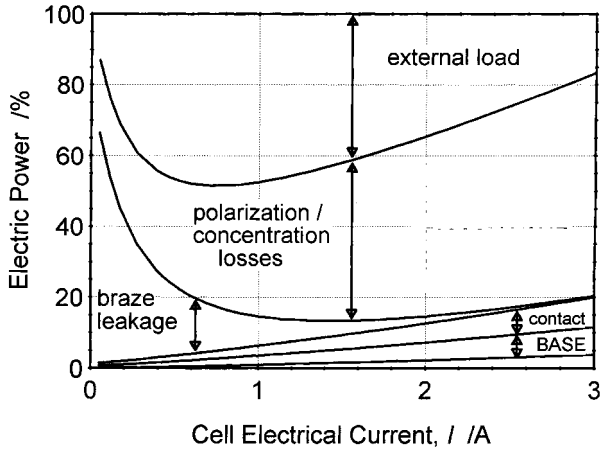

Fig. 8. Fraction of electrical loss processes in PX-3G cell. $T_{hot} = 1123$ K and $T_{cd} = 553$ K.

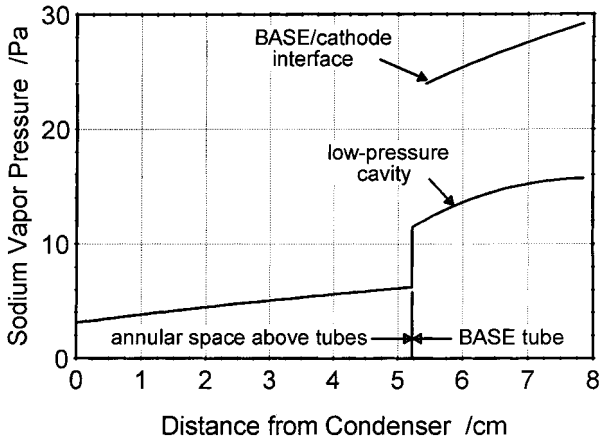

Fig. 10. Sodium vapour pressure on low-pressure side of PX-3G cell. $T_{hot} = 1123$ K, $T_{cd} = 553$ K, $I = 1.8$ A.

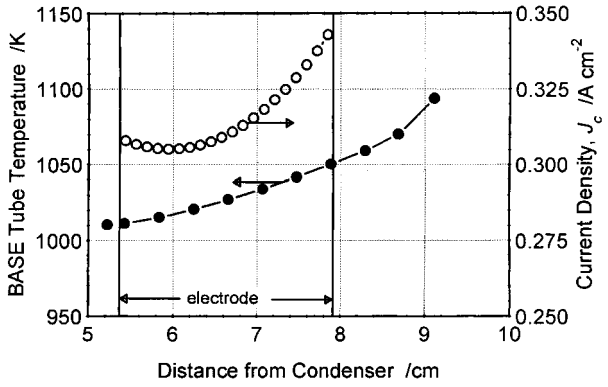

Fig. 11. BASE tubes temperature and current density in PX-3G cell. $T_{hot} = 1123$ K, $T_{cd} = 553$ K, $I = 1.8$ A.

The calculated current density in PX-3G at an external load resistance $R_L = 1.14\,\Omega$ ($I = 1.8$ A) is shown in Figure 11, along with the predicted axial temperature distribution along the BASE tubes. The current density, J_c, along the cathode electrode only changed by up to 12%, and had a minimum of 0.307 A cm^{-2} near the mid plane of the electrode. This axial distribution of J_c resulted from the combined effects of the axial distributions of sodium vapour pressure on the cathode side and of the BASE temperature. The temperature of the electrode varied between 1012 K and 1051 K (Figure 11, Table 1). The Mo current collection grids on the inside and outside surfaces of the BASE tubes increased the effective axial conductance of the solid electrolyte membrane by two orders of magnitude, limiting the temperature drop along the electrode portion of the BASE tubes to only 39 K. Figure 11, however, indicates a larger temperature drop of about 43 K along the braze section of the BASE tubes, which is not covered by the current collectors. The calculated maximum temperature of the braze in the PX-3G cell was 1094 K when operated at the peak electrical power (Figure 11, and Table 1).

Parametric analyses were performed to investigate the effects of the contact losses, leakage current, and charge-exchange/concentration losses on the performance of the PX-3G cell (Figure 1). The analyses were performed at fixed $T_{hot} = 1123$ K and condenser temperature, $T_{cd} = 553$ K. The values of R'_{cont}, R_{leak} and B were varied independently, to quantify their individual effect on the I/V characteristic and electrical power output of the PX-3G cell. Results are presented and discussed next.

3.2. *Effect of internal ohmic losses*

Figure 12 shows the effect of decreasing the contact resistance on the performance parameters of the PX-3G cell. Since ohmic losses increase with cell current, the effect of R'_{cont} is most noticeable in the low voltage region of the I/V characteristic. Higher values of R'_{cont} reduce the peak electric power of the cell and shift it to lower cell current (or higher cell terminal voltage) and vice versa (Figure 12(a)). Doubling R'_{cont} (from 0.06 to

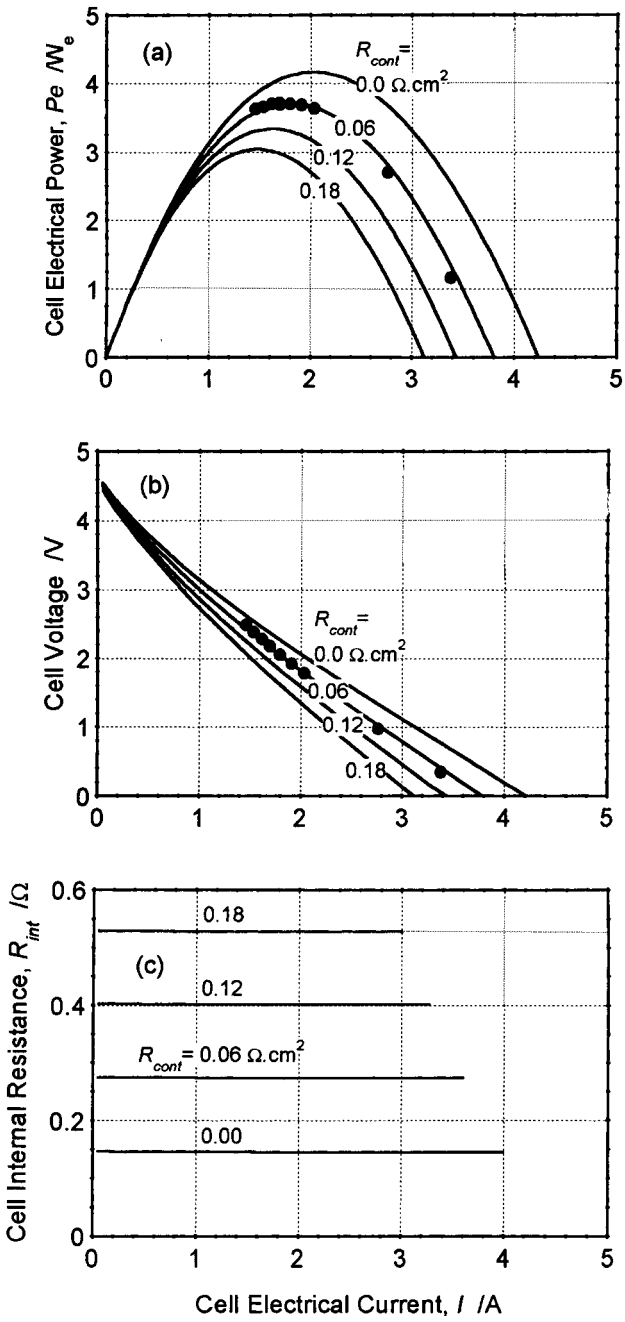

Fig. 12. Effect of contact resistance on performance of PX-3G cell. $T_{hot} = 1123$ K, $T_{cd} = 553$ K. Key for (a) and (b): (●) experiment and (——) model.

0.12 Ω cm^2) increases the cell internal resistance by 46% (from 0.274 to 0.40 Ω), and decreases the cell peak electric power by 10%, to 3.32 W$_e$.

The internal electric losses of the cell increased linearly with R'_{cont} (Figure 12(c)). The PX-3G cell, which has six 0.508 mm thick BASE tubes, and 25.4 mm long TiN electrodes, had a predicted internal resistance of 0.274 Ω (Figure 12(c)). The components of the cell internal resistance were: (a) the ionic resistance of the BASE, which is proportional to the β''-alumina solid electrolyte thickness (39.3% of R_{int}); (b) the contact resistances between the BASE and the metallic electrodes, and between the electrodes and the current

collectors (42.9% of R_{int}); (c) the ohmic losses in the 60-mesh, molybdenum current collectors (10.7% of R_{int}); and (d) the ohmic losses in the connecting leads (7.1% of R_{int}) (Table 1).

3.3. *Effect of leakage losses*

Figure 13 shows the predicted leakage current I_{leak} through the metal-ceramic braze in the PX-3G cell 1 as a function of cell current, I. At the peak electric power of the cell, $I = 1.8$ A and $I_{leak} = 0.12$ A per BASE tube. When the external load resistance, R_L increased, the cell electric current, I decreased, and the increased voltage drop between the anode and cathode electrodes (Figure 13(b)) stimulated larger leakage current (or leakage losses) through the metal–ceramic braze joint, between the BASE tubes and the stainless steel support plate. When R_L decreased, I increased and the voltage difference between the anode and cathode electrodes decreased, causing I_{leak}, and hence, leakage losses, to decrease (Figure 13(c)).

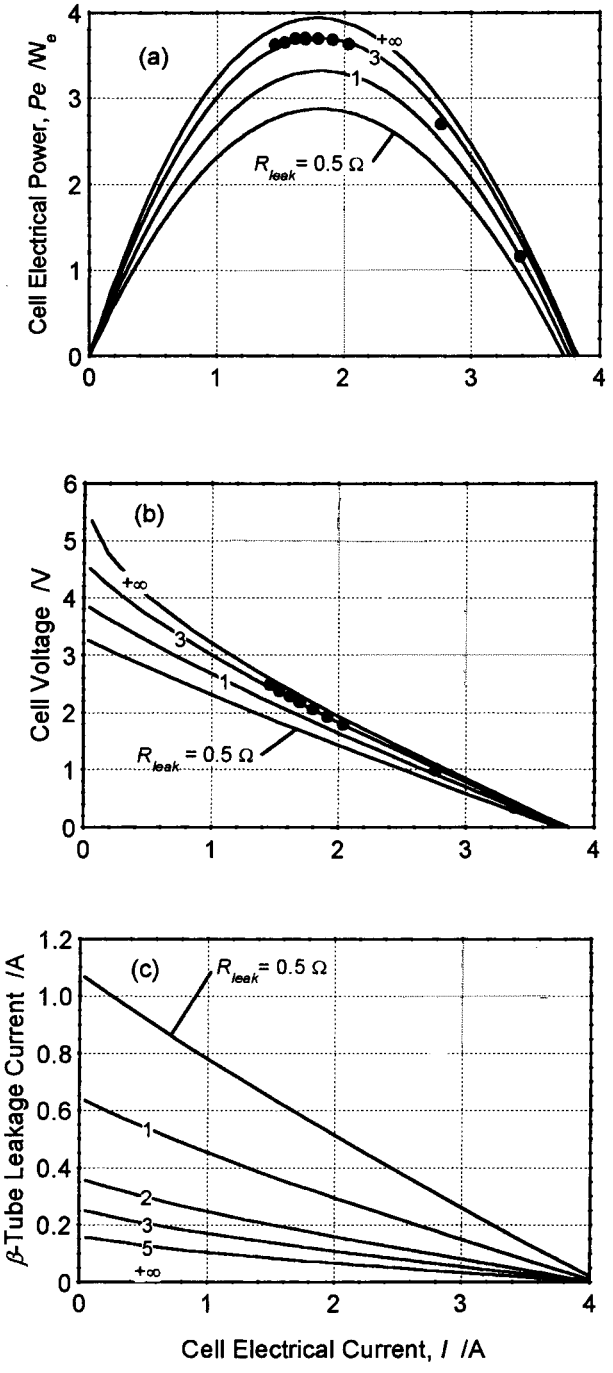

Fig. 13. Effect of braze leakage current on performance of PX-3G cell. $T_{hot} = 1123$ K, $T_{cd} = 553$ K. Key for (a) and (b): (●) experiment and (——) model.

Figure 13 also shows the effect of R_{leak} on the performance of the PX-3G cell and on the leakage current through the BASE brazes. Again, the influence of R_{leak} is more noticeable in the high voltage region of the I/V characteristic. The leakage losses lower the cell electrical power output, but insignificantly affects the cell current corresponding to the peak electric power (Figure 13(a)). The latter is a clear and accurate indicator of the existence of leakage losses in the cells.

3.4. *Effect of concentration and charge-exchange polarization losses*

The charge-exchange coefficient, B, was varied between 50 A $K^{1/2}$ Pa^{-1} m^{-2} and $+\infty$ (theoretical limit), and the corresponding load electrical power and voltage were calculated and plotted in Figures 14(a) and (b). As shown in these Figures, the exchange current coefficient, B affects the entire I/V characteristic of the cell. Higher B values shift the I/V characteristic in parallel fashion to the upper right (i.e., toward higher current and voltage) and vice versa.

As shown in Figure 14(a), the PX-3G cell delivered a peak load power of 3.7 W_e when operated at hot and cold side temperatures of 1123 K and 553 K, respectively. Model results matched the experimental data when $B = 75$ A $K^{1/2}$ Pa^{-1} m^{-2} was used. This value is typical of that of TiN electrodes used in the PX-3G cell [9]. Values in the range 120–200 A $K^{1/2}$ Pa^{-1} m^{-2} have, however, been measured for uncontaminated Rh_2W electrodes [14].

Figures 14(a) and (b) show the effect of increasing B on the cell peak power output and voltage. A PX-3G cell with Rh_2W electrodes could have delivered a peak load power in the range 4.2–4.6 W_e (14–25% more than the PX-3G cell with TiN electrodes). Even higher cell performance could be obtained with B values as high as 400 A $K^{1/2}$ Pa^{-1} m^{-2}, using oxide-enhanced Mo electrodes or possibly new refractory materials such as TiB_2 [15]: a peak power of 5.0 W_e, which is 35% higher than that of the PX-3G cell with TiN electrodes. In addition to demonstrating high performance, the electrodes must also demonstrate structural stability of operation at high temperatures, for long period of times, commensurate with the expected mission lifetime (14 years for the Pluto/Kuiper Express, and six years for the Europa Orbiter mission).

Figure 14(c) shows that increasing B from 75 to 400 A $K^{1/2}$ Pa^{-1} m^{-2} reduces the polarization/concen-

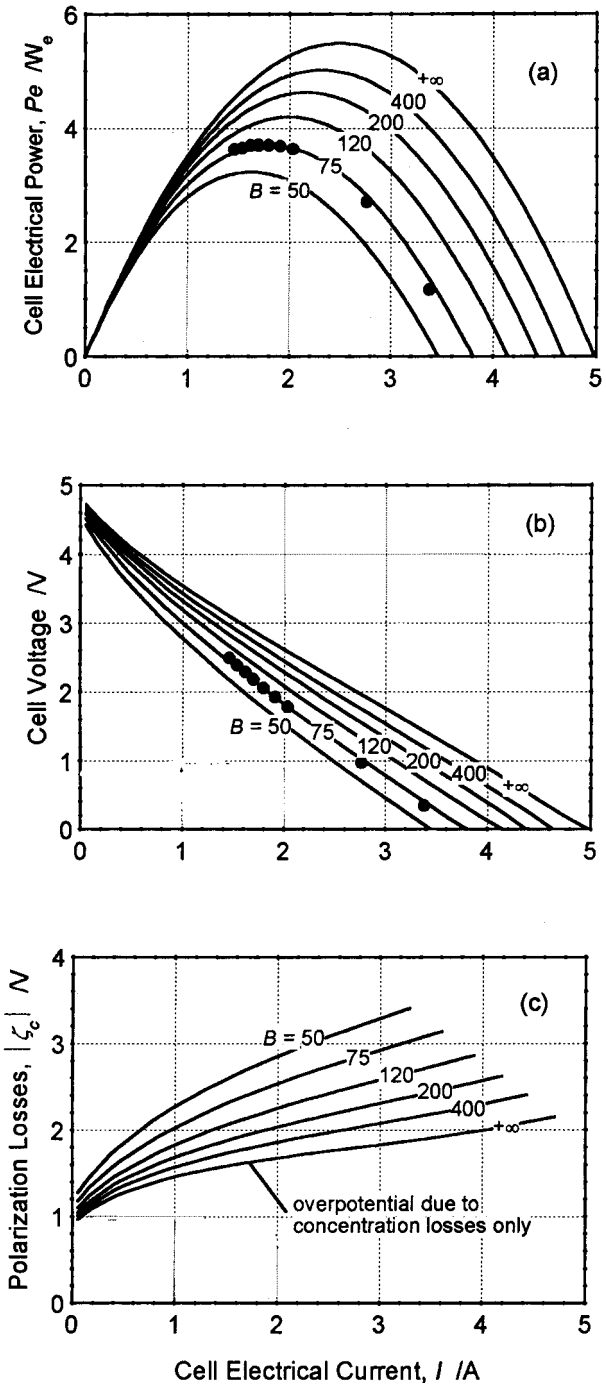

Fig. 14. Effect of charge-exchange coefficient, B, on performance of PX-3G cell. $T_{hot} = 1123$ K, $T_{cd} = 553$ K. Key for (a) and (b): (●) experiment and (——) model.

tration overpotential in the cell by about 30%, resulting in a 35% increase in the cell peak electric power (from 3.7 to 5.0 W_e). However, even if a perfect electrode was used (i.e., $B = +\infty$), the overpotential would not be zero (1.74 V at the peak power, corresponding to $I = 2.5$ A), because of the concentration losses (or effect of vapour pressure losses in the low pressure cavity; Equation 3(b), Figure 14(c)). The PX-3G cell has a predicted total geometric factor $G = 192$ on the low-pressure side [4]. The total vapour pressure losses comprise those due to evaporation of sodium at the BASE/electrode interface ($G_{ev} = 40$), vapour transpiration through TiN cathode electrode ($G_E = 50$), vapour flow between electrode surface and cell condenser ($G_{fl} = 82$), and condensation of sodium vapour ($G_{cd} = 20$). Therefore, the pressure drop through the electrode contributed only $(50/192) = 26\%$ of the total vapour pressure losses in the low-pressure cavity.

4. Summary and conclusion

To quantify the contribution of the various electric losses in vapour anode, multitube AMTEC cells, a two-dimensional electric model was developed, which included four options of current collector configurations: tie wires wrapped around the BASE tube, a metal sponge or a wire screen mesh held in place by tie wires, or a single helical wire. The current collector resistances were calculated using a conservative approach, by assuming a current collection path, and integrating the Joule losses along the path.

The present model accounted for nonuniform axial temperature and vapour pressure profiles along the BASE tubes/electrodes; concentration and charge-exchange polarization losses at the BASE/electrode interfaces; ionic losses of the BASE; contact losses between electrodes and current collectors; leakage losses between anode and cathode electrodes through the BASE braze joint; sheet losses in the plane of the electrodes; and radial and axial electrical losses in the current collector networks, including those in the bus wires and the conductor leads to the load. The model was successfully integrated into APEAM, a full cell model. Results of several PX-series cells which have been tested at AFRL showed that the electrical losses in the current collector networks and the connecting leads were negligible. However, the polarization/concentration losses in the TiN electrodes were the major loss, amounting to 25–50% of the theoretical Nernst electric power. Contact losses, combined with BASE ionic losses, amounted to less than 16% of the theoretical Nernst power.

The cell model results matched the experimental data of the PX-3G cell when $B = 75$ A $K^{1/2}$ Pa^{-1} m^{-2}, $R'_{cont} = 0.06\ \Omega\ cm^2$ and $R_{leak} = 3\,\Omega$. The PX-3G cell delivered a peak power of 3.7 W_e at $I = 1.8$ A and overpotential of 2.4 V, when operated at $T_{hot} = 1123$ K and $T_{cd} = 553$ K. This cell had six 0.508 mm thick BASE tubes, and 25.4 mm long TiN electrodes, and a predicted internal resistance, $R_{int} = 0.274\,\Omega$. The ionic resistance of the BASE contributed 39.3% of R_{int}, while the contact resistances between the BASE and the metallic electrodes, and between the electrodes and the current collectors contributed 42.9% of R_{int}. The ohmic losses in the current collectors and leads constituted the remaining of R_{int}.

Results also showed that a PX-3G cell with Rh_2W or other advanced electrodes, exhibiting B values in the range 120–200 A $K^{1/2}$ Pa^{-1} m^{-2}, could have delivered a

peak load electrical power in the range 4.2–4.6 W_e (which is 14–25% more than the PX-3G cell with TiN electrodes). However, even if a perfect electrode were used (i.e., $B = +\infty$), the overpotential would not reduce to zero, because of the concentration losses or the effect of sodium vapour pressure on the cathode side of the BASE tube. The PX-3G cell had a predicted total geometric factor $G = 192$ for vapour pressure losses. The pressure drop through the TiN electrode contributed only 26% of the total vapour pressure losses in the low-pressure cavity.

Acknowledgements

This research is funded by the Space Vehicles Technologies Directorate of the Air Force Research Laboratory, Kirtland Air Force Base, New Mexico, under contract F29601-96-K-0123, to the University of New Mexico's Institute for Space and Nuclear Power Studies.

References

1. J. Merrill, M.J. Schuller and L. Huang, Proceedings of the Space Technology and Applications International Forum (STAIF-98), CONF-980103 (edited by M.S. El-Genk), American Institute of Physics, New York, AIP Conference Proceedings no. 420, 3 (1998) 1613–1620.
2. M.S. El-Genk and J.-M. Tournier, Proceedings of the 5th European Space Power Conference (ESPS-98), held 21–25 Sept. 1998, in Tarragona, Spain, SP-416, European Space Agency Publications Division, Paper 1046 (1998) 257–264.
3. J.-M. Tournier and M.S. El-Genk, Proceedings of the 33rd Intersociety Energy Conversion Engineering Conference, American Nuclear Society, Chicago, IL, Paper 98057 (1998).
4. J.-M. Tournier and M.S. El-Genk, Proceedings of the Space Technology and Applications International Forum (STAIF-98), CONF-980103 (edited by M.S. El-Genk), American Institute of Physics, New York, AIP Conference Proceedings no. 420, 3 (1998) 1595–1606.
5. J.-M. Tournier and M.S. El-Genk, Proceedings of the Space Technology and Applications International Forum (STAIF-98), CONF-980103, (edited by M.S. El-Genk), American Institute of Physics, New York, AIP Conference Proceedings no. 420, 3 (1998) 1552–1563.
6. T. Cole, *Science* **221** (4614) (1983) 915–920.
7. R.M. Williams, M.E. Loveland, B. Jeffries-Nakamura, M.L. Underwood, C.P. Bankston, H. Leduc and J.T. Kummer, *J. Electrochem. Soc.* **137**(6) (1990) 1709–1716.
8. M.L. Underwood, R.M. Williams, M.A. Ryan, B. Jeffries-Nakamura and D. O'Connor, Proceedings of the 9th Symposium on Space Nuclear Power Systems, CONF-920104, American Institute of Physics, New York, AIP Conference Proceedings no. 246, 3 (1992) 1331–1337.
9. M.A. Ryan, R.M. Williams, M.L. Homer, W.M. Phillips, L. Lara and J. Miller, Proceedings of the Space Technology and Applications International Forum (STAIF-98), CONF-980103 (edited by M. S. El-Genk), American Institute of Physics, New York, AIP Conference Proceedings no. 420, 3 (1998) 1607–1612.
10. R.K. Sievers, R.A. Markley, J.E. Schmidt, N. Weber, J.R. Rasmussen, S.L. Olsen and T.K. Hunt, 'Space Nuclear Power Systems 1988' (edited by M.S. El-Genk and M.D. Hoover), Orbit Book Company, Malabar, FL (1989), Chapter 63, 9 (1988) 531–540.
11. K. Tanaka, A. Negishi and T. Masuda, Proceedings of the 27th Intersociety Energy Conversion Engineering Conference, Paper 929008, Society of Automotive Engineers, 3 (1992) 13–18.
12. J.-M. Tournier and M.S. El-Genk, Proceedings of the Space Technology and Applications International Forum (STAIF-98), CONF-980103 (edited by M.S. El-Genk), American Institute of Physics, New York, AIP Conference Proceedings no. 420, 3 (1998) 1576–1585.
13. M. Steinbruck, V. Heinzel, F. Huber, W. Peppler, H. Will and M. Voss, Proceedings of the 28th Intersociety Energy Conversion Engineering Conference, Paper 93108, American Chemical Society, 1 (1993) 799–807.
14. M.A. Ryan, B. Jeffries-Nakamura, R.M. Williams, M.L. Underwood, D. O'Connor and S. Kikkert, Proceedings of the 27th Intersociety Energy Conversion Engineering Conference, Paper 929007, Society of Automotive Engineers, 3 (1992) 7–12.
15. Q. Fang and R. Knödler, *J. Materi. Sci.* **27** (1992) 6725–6729.